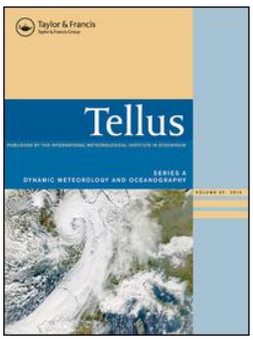

Tellus A: Dynamic Meteorology and Oceanography

ISSN: (Print) 1600-0870 (Online) Journal homepage: http://www.tandfonline.com/loi/zela20

Relative strength of the Antarctic Circumpolar Current and Atlantic Meridional Overturning Circulation

David P. Marshall & Helen L. Johnson

To cite this article: David P. Marshall & Helen L. Johnson (2017) Relative strength of the Antarctic Circumpolar Current and Atlantic Meridional Overturning Circulation, Tellus A: Dynamic Meteorology and Oceanography, 69:1, 1338884, DOI: 10.1080/16000870.2017.1338884

To link to this article: http://dx.doi.org/10.1080/16000870.2017.1338884

Published online: 26 Jun 2017.

Tellus
SERIES A
DYANAMIC
METEOROLOGY
AND OCEANOGRAPHY
PUBLISHED BY THE INTERNATIONAL METEOROLOGICAL INSTITUTE IN STOCKHOLM

Relative strength of the Antarctic Circumpolar Current and Atlantic Meridional Overturning Circulation

By DAVID P. MARSHALL[1]* and HELEN L. JOHNSON[2], [1]*Department of Physics, University of Oxford, Oxford, UK;* [2]*Department of Earth Sciences, University of Oxford, Oxford, UK*

(Manuscript received 22 December 2016; in final form 29 May 2017)

ABSTRACT

A simple relationship, based on thermal wind balance, is derived that relates the relative strength of the Antarctic Circumpolar Current (ACC) and Atlantic Meridional Overturning Circulation (AMOC) to the ratios of three depth scales: the e-folding depth of the global stratification, the depth of maximum overturning streamfunction and the maximum depth of the ACC. For realistic values of these depth scales, the relationship predicts a factor 8 ± 4 difference in the volume transports of the ACC and AMOC, consistent with the observation-based ratio of 8 ± 2.

Keywords: ocean currents, volume transports, hydrography, thermal wind, meridional boundaries

1. Introduction

Two of the most important components of the global ocean circulation are the Atlantic Meridional Overturning Circulation (AMOC) and the Antarctic Circumpolar Current (ACC). The AMOC is responsible for a large fraction of the poleward heat transport in the North Atlantic (Johns et al., 2011) and for the asymmetry in poleward heat transport between the Atlantic and Pacific (Trenberth and Caron, 2001). The AMOC has been continuously monitored at 26.5N since 2004 and transports 17.2 ± 4.4 Sv of warm, buoyant water northward, with compensating southward flow of cold, dense water at depth (McCarthy et al., 2015), where the uncertainty represents the standard deviation of 10-day-filtered data. The ACC has the largest volume transport of any ocean current and its strength is closely related to global stratification and heat content (Gnanadesikan and Hallberg, 2000). The ACC has been monitored through a repeat hydrographic section across Drake Passage in most summers since 1993, and transports a much larger 137 ± 7 Sv around Antarctica, neglecting any contribution from the bottom flow. Here, the uncertainty represents the standard deviation between the 16 contributing hydrographic sections (Meredith et al., 2011). In this short contribution, we present a diagnostic relation, based on thermal wind balance, for the relative volume transport of these two currents.

The AMOC and ACC are intimately coupled. This coupling is most explicit in the simple conceptual model of Gnanadesikan (1999) for the global pycnocline, and its subsequent application to the ACC by Gnanadesikan and Hallberg (2000), Allison et al. (2010, 2011), Munday et al. (2011). In this model, sketched in Fig. 1, the depth of the global pycnocline, h, is controlled by a balance between water mass transformations associated with Southern Ocean Ekman transport, Southern Ocean eddies, diapycnal mixing and the AMOC. As discussed by Johnson et al. (2007), the volume transport of the AMOC in this model is given by

$$T_{\mathrm{AMOC}} \approx \frac{g' h^2}{2 f_{\mathrm{AMOC}}}, \tag{1}$$

obtained by integrating the northward thermal wind across the basin, assuming that the pycnocline outcrops (or nearly outcrops) at the western boundary – see Fig. 1b in Johnson et al. (2007) – and that the velocity is weak in the abyssal layer. Here, f_{AMOC} is the Coriolis parameter at the outcrop latitude and g' is the reduced gravity. Similarly, as discussed by Allison et al. (2010), the baroclinic volume transport of the ACC, neglecting any flow in the abyssal layer, is given by

$$T_{\mathrm{ACC}} \approx -\frac{g' h^2}{2 f_{\mathrm{ACC}}}, \tag{2}$$

where it is assumed that the pycnocline outcrops to the south around Antarctica and where f_{ACC} is a typical Coriolis parameter at the latitude of the ACC, e.g. at Drake Passage. Since $|f_{\mathrm{AMOC}}| \sim |f_{\mathrm{ACC}}|$, and assuming the same g' in (1) and (2), it

*Corresponding author. e-mail: david.marshall@physics.ox.ac.uk

Citation: Tellus A: 2017, **69**, 1338884, https://doi.org/10.1080/16000870.2017.1338884

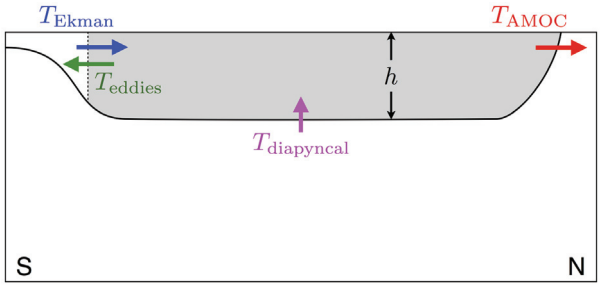

Fig. 1. Schematic of the two layer model of Gnanadesikan (1999) for the depth, h, of the global pycnocline. T_{Ekman}, T_{eddies}, $T_{\text{diapycnal}}$ and T_{AMOC} are the water mass transformations between the two layers associated with northward Ekman transport in the Southern Ocean, Southern Ocean eddies, diapycnal mixing in the ocean interior, and North Atlantic Deep Water formation, respectively.

follows that the volume transports of the AMOC and ACC are broadly similar in the simple Gnanadesikan model.

Reconciling this result with the factor 8 ± 2 difference between the observed mean volume transports of the AMOC and ACC requires us to consider, in more detail, the vertical structure of the stratification and the currents. Specifically, for both (1) and (2) to apply to AMOC and ACC, respectively, it is necessary to choose different values of g' and/or h for each. Extensions of Gnanadesikan's model to multiple layers have been developed by Radko and Kamenkovich (2011), Nikurashin and Vallis (2012), and Shakespeare and Hogg (2012). In particular, Shakespeare and Hogg (2012) derive a relationship between the ACC volume transport and the sum of the Southern Ocean Ekman transport and abyssal overturning; the ACC volume transport differs from the AMOC volume transport in their model. All three of these models predict how different aspects of the global stratification and circulation vary with surface wind and buoyancy forcing, albeit reliant on uncertain physical parameters such as the Southern Ocean eddy diffusivity. In this manuscript, however, our aim is to show that a simpler, diagnostic relationship exists, independent of the forcing mechanism, between the ratio of the ACC and AMOC volume transports and the ratios of three simple depth scales.

The manuscript is structured as follows. In Section 2, we motivate our model by examining variations in the depth of neutral density surfaces in the World Ocean Circulation Experiment (WOCE) climatology. In Section 3, we then derive a simple relationship between the volume transport of the ACC and the volume transport of the AMOC, in terms of three fundamental depth scales: the maximum depth of the ACC, the depth of the maximum AMOC streamfunction and the e-folding depth of the global stratification. In Section 4, we determine the three depth scales from WOCE hydrographic data, before showing in Section 5 that the predicted ratio between the volume transports of the ACC and AMOC is 8 ± 4, consistent with the observation-based estimate. Finally in Section 6, we discuss the limitations of our approach and the implications of our results for understanding how the ocean circulation may have changed over geological time.

2. WOCE climatology

In this section, we discuss the extent to which the observed structure of the global ocean differs from the simple two-layer conceptual framework of Gnanadesikan (1999), using climatological hydrographic data from the WOCE Atlantic Ocean Atlas (Koltermann et al., 2011).

Various sections of neutral density are shown in Fig. 2. The lower section (a composite from the A23 and A16 sections) extends northward from Antarctica to the Greenland Sea through the centre of the Atlantic. The most notable feature, consistent with Gnanadesikan's model, is that most of the neutral density surfaces outcrop to the south (indeed, the densest surfaces outcrop in the Ross Sea, but this is not apparent from this particular two-dimensional section), whereas the neutral density surfaces are remarkably flat to the north of the ACC (north of about 40°S). The neutral density surfaces are even flatter at the eastern boundary, as illustrated in Fig. 3 and central to our analysis. The reason for the remarkably flat isopycnals, away from the western boundary, is the strong tendency of eastern boundary waves to remove any meridional pressure gradients and hence flatten the neutral surfaces, and for long Rossby waves to propagate these conditions westward into the basin interior (Johnson et al., 2007; Marshall and Johnson, 2013).

The upper central panels show the variation of neutral density along two additional sections crossing the ACC (A21 across Drake Passage and A12 between Antarctica and the southern tip of Africa). All three sections reveal a similar structure with almost all isopycnals outcropping to the south from depths of about 4 km. We define this maximum depth of the ACC as h_{ACC}, above which the isopycnals slope and there is a thermal wind shear.

Plotted in the upper left panel of Fig. 2 is a zonal section (A02) across the North Atlantic from the Grand Banks to the Irish Sea. The neutral density surfaces are relatively flat, except adjacent to the western boundary where they slope steeply. In contrast to the Southern Ocean, only the neutral density surfaces with an open ocean depth shallower than about 1 km outcrop at the western boundary. Further evidence for this asymmetry between outcropping in the Southern Ocean and in the high-latitude North Atlantic is presented in Fig. 3, which shows the neutral density at 0.5 and 1.5 km depths. At 0.5 km, dense water is found in both the Southern Ocean and high-latitude North Atlantic; in contrast at 1.5 km, dense water is found in the Southern Ocean but not in the high-latitude North Atlantic.

The reason for these differences can be understood by thinking about the density classes in which North Atlantic Deep Water is formed and how this relates to the depth of the maximum overturning streamfunction in the Atlantic. The lightest North

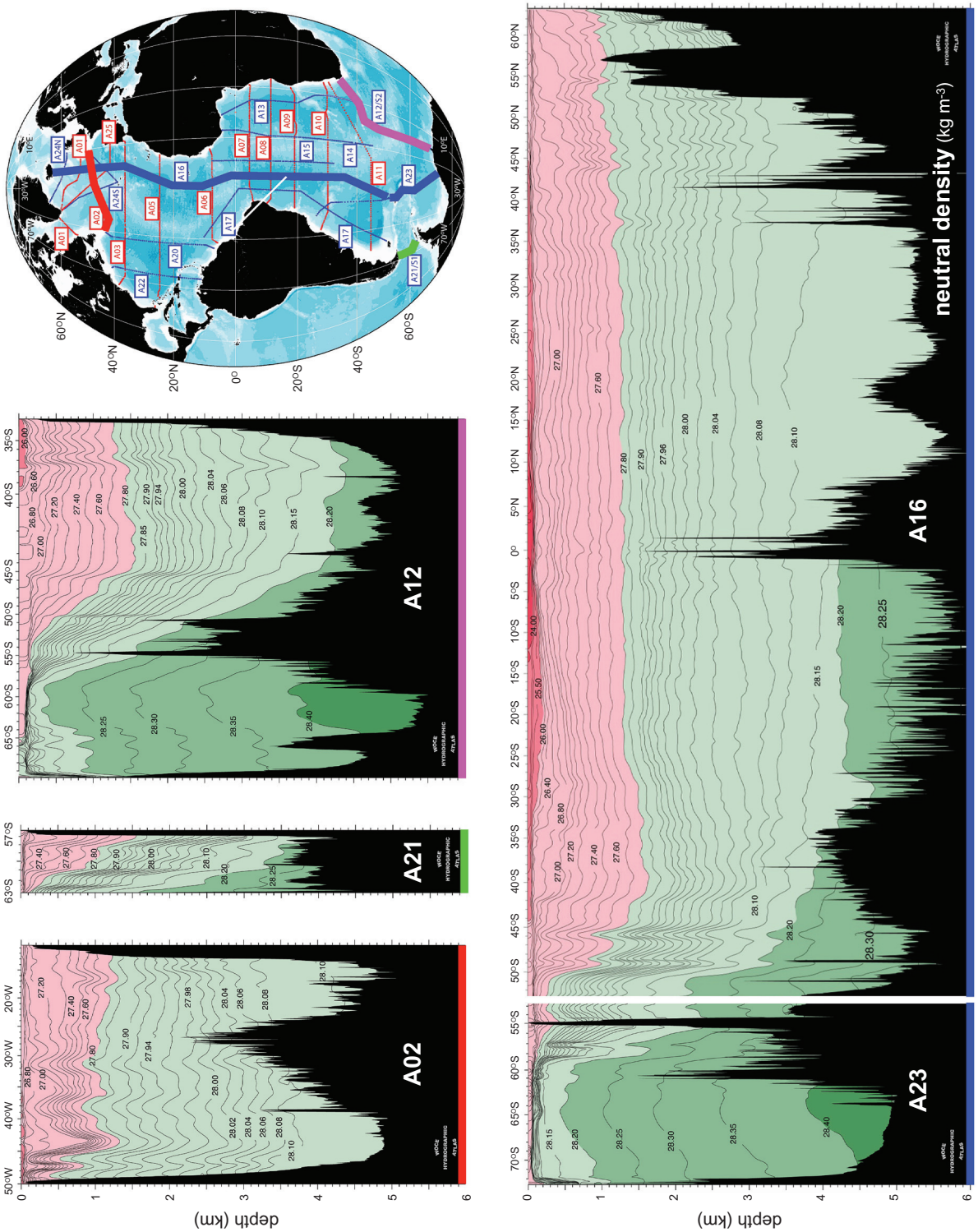

Fig. 2. Neutral density sections from WOCE in the Atlantic sector, adapted with permission from the WOCE Atlantic Ocean Atlas (Koltermann et al., 2011). The coloured bars at the bottom of each section correspond to the coloured lines on the map (upper right panel). The lower section is a composite between the A23 and A16 sections.

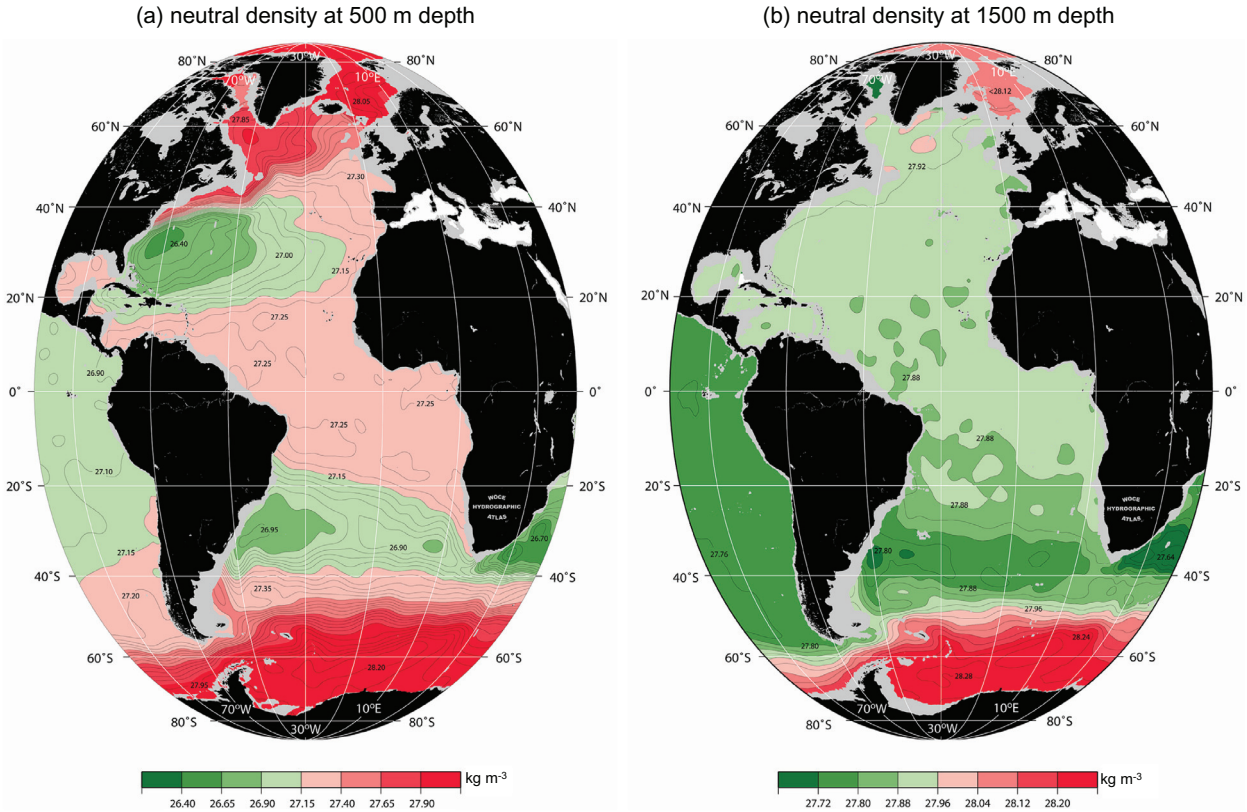

Fig. 3. Neutral density at (a) 500 m and (b) 1500 m, reproduced with permission from the WOCE Atlantic Atlas (Koltermann et al., 2011).

Atlantic Deep Water is formed in the Labrador Sea, and hence the interface between this water mass and the lighter water above sets the depth of maximum overturning. By definition, this must coincide with the neutral density surface that outcrops at the southern margin of the Labrador Sea (the A02 section in Fig. 2). The depth of maximum AMOC streamfunction is at about 1 km depth (e.g. Lumpkin and Speer, 2007; Smeed et al., 2014), consistent with the depth of outcropping neutral density surfaces in the A02 section. We define this depth of the maximum AMOC streamfunction as h_{AMOC}.

In summary, a likely explanation for the vastly different volume transports of the ACC and AMOC is the vastly different depth scales over which neutral density surfaces outcrop, h_{ACC} and h_{AMOC}. At the depth h_{ACC} in the Southern Ocean, we anticipate that the circumpolar circulation will be weak, for example, due to blocking effects of the bottom topography. Likewise, at the depth h_{AMOC} in the high-latitude North Atlantic, the basin-integrated meridional flow vanishes. As we will show in the following section, and consistent with the results of Shakespeare and Hogg (2012), these different depth scales impose different boundary conditions on the thermal wind velocities that set the volume transports of the ACC and AMOC.

3. Relationship between ACC and AMOC volume transports

A simple equation for the relative volume transports of the ACC and AMOC (Fig. 4a) is now derived using four simple ingredients: (i) thermal wind balance; (ii) the observation that the stratification is near constant with latitude along the eastern boundary of the Atlantic; (iii) the different depth scales, h_{ACC} and h_{AMOC}, from which isopycnals outcrop at high latitudes in the Southern Ocean and North Atlantic; (iv) an imposed exponential variation of neutral density with depth.

The latter is imposed in order to reduce the complexity of the relationship and allow the vertical structure of the global stratification to be described through a single parameter. Thus the neutral density is modelled as

$$\gamma_n = \gamma_\infty - (\Delta\gamma)_0\, e^{z/h_{\mathrm{strat}}}, \tag{3}$$

where z is the height, with the sea surface at $z = 0$ and h_{strat} is the e-folding depth of the stratification. The parameter γ_∞ represents the asymptotic value of the neutral density at large

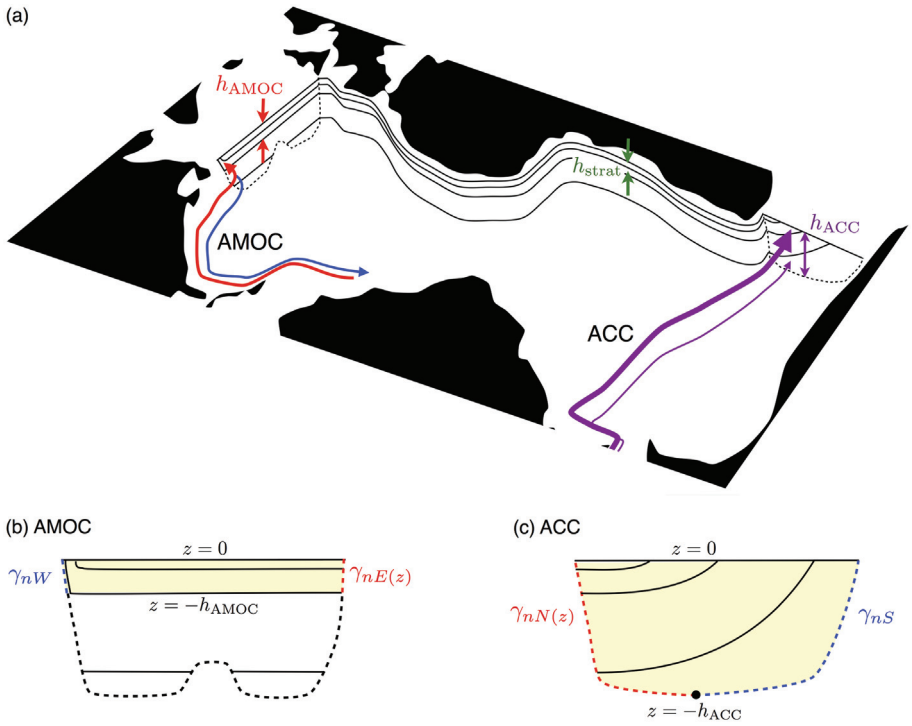

Fig. 4. (a) Schematic diagram showing the key elements of the thermal wind model. The solid black lines indicate the neutral density surfaces which are flat along the eastern boundary of the Atlantic but slope and can outcrop in the sections across the Southern Ocean and North Atlantic. The dashed lines represent the sloping boundaries to the north and south of the Southern Ocean section, and to the east and west of the North Atlantic section. The three depth scales h_{strat}, h_{ACC} and h_{AMOC} are also indicated – see main text for details. The long solid purple arrows symbolise the ACC, and the long solid red and blue arrows symbolise the upper and lower limbs of the AMOC. (b) Schematic of the model across the North Atlantic section. The strength of the AMOC is set by integrating the thermal wind relation between the sloping eastern (dashed red) and western (dashed blue) boundaries, from the assumed level of no motion at $z = -h_{\mathrm{AMOC}}$ to the surface $z = 0$. (c) Schematic of the model across the Southern Ocean section. The strength of the ACC is set by integrating the thermal wind relation between the sloping northern (dashed red) and southern (dashed blue) boundaries, from $z = -h_{\mathrm{ACC}}$ to the surface $z = 0$.

depths and $(\Delta\gamma)_0$ is the difference between this and the surface neutral density. The extent to which (3) can model the observed global climatological stratification is assessed in Section 4.

We assume that the flow satisfies the thermal wind relation, consistent with the horizontal and vertical momentum equations being well approximated by geostrophic and hydrostatic balance. Moreover, we assume that the thermal wind relation can be written in terms of neutral density,

$$\frac{\partial u}{\partial z} = \frac{g}{\rho_0 f}\frac{1}{R}\frac{\partial \gamma_n}{\partial \theta}, \qquad \frac{\partial v}{\partial z} = -\frac{g}{\rho_0 f}\frac{1}{R\cos\theta}\frac{\partial \gamma_n}{\partial \phi}, \tag{4}$$

were u and v are the zonal and meridional velocity components, g is the gravitational acceleration, ρ_0 is a reference density, $f = 2\Omega\cos\theta$ is the Coriolis parameter, Ω is the Earth's rotation rate, R is the radius of the Earth, θ is latitude and ϕ is longitude. The use of neutral, rather than in-situ, density in (4) introduces a small error relative to other assumptions made.

3.1. ACC

The thermal wind relation (4) can be used to estimate the ACC volume transport by assuming the density surfaces outcrop to the south above the depth h_{ACC}, at which the flow is vanishingly small, as discussed in Section 2. We also neglect the small variations in the Coriolis parameter, f_{ACC}, across the ACC. Integrating (4) from Antarctica to the southern tip of Africa, we obtain

$$\begin{aligned} T_{\mathrm{ACC}} &= \int_{-h_{\mathrm{ACC}}}^{0}\int_{\theta_S}^{\theta_N} u\, R\, \mathrm{d}\theta\, \mathrm{d}z \\ &= -\int_{-h_{\mathrm{ACC}}}^{0}\int_{\theta_S}^{\theta_N} z\frac{\partial u}{\partial z}\, R\, \mathrm{d}\theta\, \mathrm{d}z \\ &= -\int_{-h_{\mathrm{ACC}}}^{0} \frac{gz}{\rho_0 f_{\mathrm{ACC}}}(\gamma_{nN} - \gamma_{nS})\, \mathrm{d}z, \end{aligned} \tag{5}$$

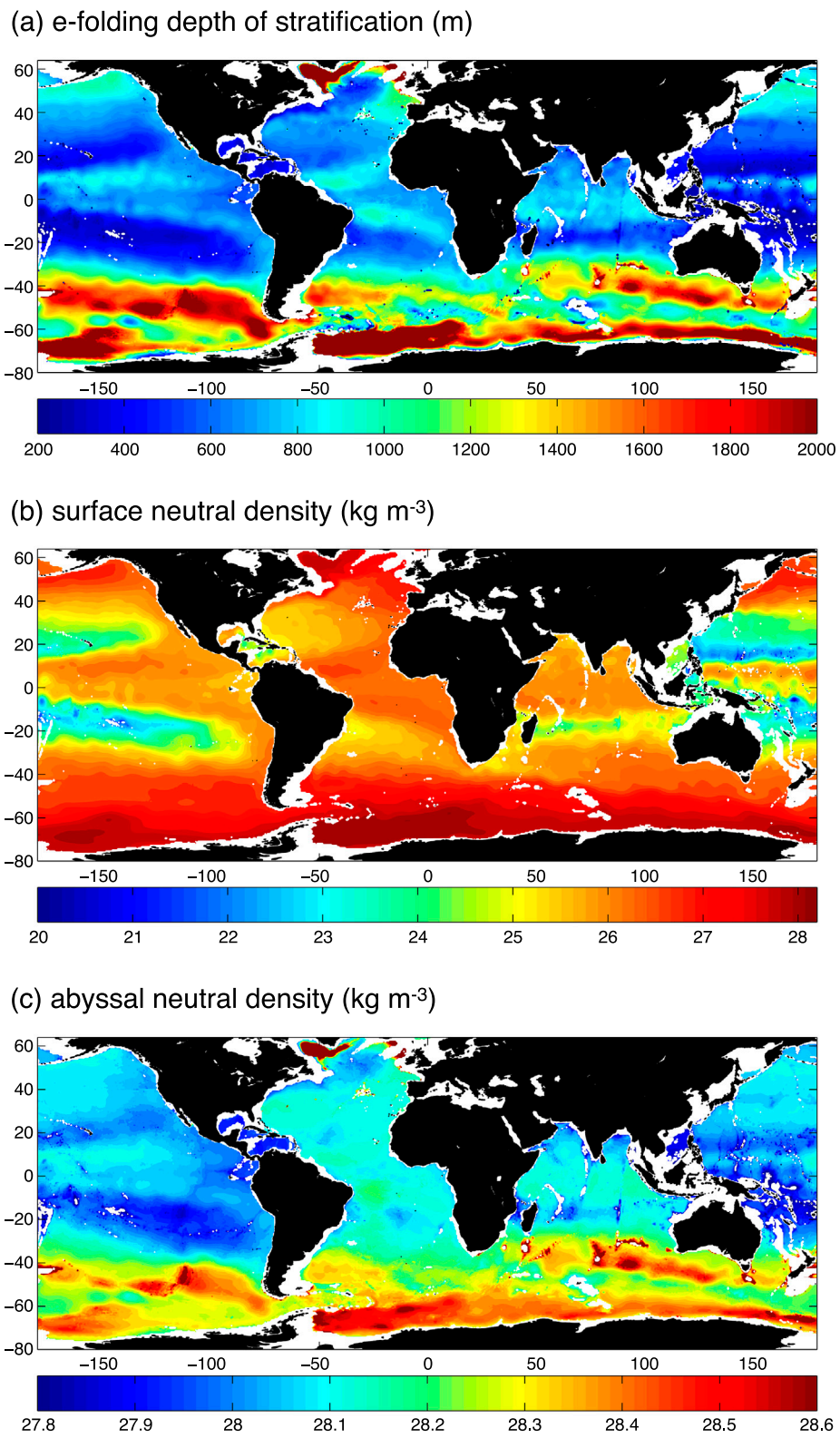

Fig. 5. The (a) e-folding depth, (b) surface neutral density and (c) asymptotic abyssal neutral density, obtained by fitting the exponential neutral density profile (3) to the WOCE climatological data of Gouretski and Koltermann (2004).

where we have used that $z = 0$ at the surface and $u = 0$ at $z = -h_{\mathrm{ACC}}$. Equation (5) demonstrates that the baroclinic volume transport of the ACC is strongly constrained by the density profiles to its north, γ_{nN}, e.g. along the sloping boundary of the southern tip of Africa, and its south, γ_{nS}, along the sloping boundary of Antartica (Munday et al., 2011), as sketched in Fig. 4c.

Consistent with the climatological hydrographic data in Fig. 2, the neutral density to the south is assumed constant above the depth h_{ACC}, where it is equal to the neutral density to the north at that depth, that is

$$\gamma_{nS}(z) = \gamma_{nN}(-h_{\mathrm{ACC}}) \quad \text{for} \quad z > -h_{ACC}. \tag{6}$$

Now substituting (6) and the exponential profile (3) for $\gamma_{nN}(z)$ into (5), we obtain

$$\begin{aligned} T_{\mathrm{ACC}} &= \frac{g\,\Delta\gamma_0}{\rho_0 f_{\mathrm{ACC}}} \int_{-h_{\mathrm{ACC}}}^{0} z \left(e^{\frac{z}{h_{\mathrm{strat}}}} - e^{-\frac{h_{\mathrm{ACC}}}{h_{\mathrm{strat}}}} \right) \mathrm{d}z \\ &= \frac{g\,\Delta\gamma_0 h_{\mathrm{strat}}^2}{\rho_0 f_{\mathrm{ACC}}} \left[1 - \left(1 + \frac{h_{\mathrm{ACC}}}{h_{\mathrm{strat}}} + \frac{h_{\mathrm{ACC}}^2}{2h_{\mathrm{strat}}^2} \right) e^{-\frac{h_{\mathrm{ACC}}}{h_{\mathrm{strat}}}} \right]. \end{aligned} \tag{7}$$

Thus, the volume transport of the ACC depends on a number of parameters multiplied by a complicated function involving just the ratio of the depths h_{ACC} and h_{strat}.

The same procedure can be applied across other ACC sections, such as Drake Passage; by continuity, the ACC volume transport through different sections can only differ by the net volume loss due to surface freshwater fluxes and the net flow through the Arctic Ocean between the Atlantic and Pacific. Here, we choose to focus on a section between Antarctica and the southern tip of Africa because this explicitly connects to the stratification on the eastern boundary of the Atlantic.

3.2. AMOC

The same approach can be applied to estimate the volume transport of the AMOC at the southern tip of the Labrador Sea, except that the thermal wind relation (4) is integrated from the depth of maximum overturning streamfunction, h_{AMOC}. At this depth, the zonally integrated flow reverses; here, we make the stronger assumption that the meridional velocity vanishes at all longitudes across the section as well as in the zonal integral. While the latter assumption cannot be justified formally, it allows us to obtain a similar prediction for the volume transport of the AMOC as that for the ACC.

Integrating (4) from the western to the eastern boundary and defining the Coriolis parameter as f_{AMOC} at this latitude, we obtain

$$\begin{aligned} T_{\mathrm{AMOC}} &= \int_{-h_{\mathrm{AMOC}}}^{0} \int_{\phi_W}^{\phi_E} v\, R\, \cos\theta \, \mathrm{d}\phi \, \mathrm{d}z \\ &= -\int_{-h_{\mathrm{AMOC}}}^{0} \int_{\phi_W}^{\phi_E} z \frac{\partial v}{\partial z} R\, \cos\theta \, \mathrm{d}\phi \, \mathrm{d}z \\ &= \int_{-h_{\mathrm{AMOC}}}^{0} \frac{gz}{\rho_0 f_{\mathrm{AMOC}}} (\gamma_{nE} - \gamma_{nW}) \, \mathrm{d}z. \end{aligned} \tag{8}$$

Equation (8) demonstrates that the volume transport of the AMOC is strongly constrained by the density profiles along the sloping boundaries to its east, γ_{nE}, and west, γ_{nW} (Fig. 4b); this is precisely the relation exploited by the RAPID-MOCHA array (Cunningham et al., 2007; McCarthy et al., 2015). The neglect of local meridional velocities at the depth h_{AMOC} is equivalent to neglecting the so-called external mode, which is large at the latitude of the RAPID-MOCHA array (26.5°N) but much smaller further north (Sime et al., 2006).

Consistent with the climatological hydrographic data, the neutral density to the east is assumed to be nearly the same as that at the southern tip of Africa, due to the absence of significant meridional neutral density gradients along the eastern boundary of the Atlantic, that is $\gamma_{nE}(z) \approx \gamma_{nN}(z)$, and $\gamma_{nE}(z)$ is given by the same exponential profile (3). In contrast to the ACC, the neutral density at the western boundary is assumed uniform above the shallower depth h_{AMOC}.

$$\gamma_{nW}(z) = \gamma_{nE}(-h_{\mathrm{AMOC}}) \quad \text{for} \quad z > -h_{\mathrm{AMOC}}. \tag{9}$$

The hydrographic data along the WOCE section A02 (Fig. 2) indicate that the neutral density is slightly higher than this assumed uniform value beneath the surface. We have tried different assumptions, such as retaining an exponential decay with depth at the western boundary, but this has a modest impact on the results.

Now substituting (9) and (3), respectively, for the western and eastern boundary density profiles in (8), we obtain

$$\begin{aligned} &T_{\mathrm{AMOC}} \\ &= -\frac{g\,\Delta\gamma_0}{\rho_0 f_{\mathrm{AMOC}}} \int_{-h_{\mathrm{AMOC}}}^{0} z \left(e^{\frac{z}{h_{\mathrm{strat}}}} - e^{-\frac{h_{\mathrm{AMOC}}}{h_{\mathrm{strat}}}} \right) \mathrm{d}z \\ &= -\frac{g\,\Delta\gamma_0 h_{\mathrm{strat}}^2}{\rho_0 f_{\mathrm{AMOC}}} \left[1 - \left(1 + \frac{h_{\mathrm{AMOC}}}{h_{\mathrm{strat}}} + \frac{h_{\mathrm{AMOC}}^2}{2h_{\mathrm{strat}}^2} \right) e^{-\frac{h_{\mathrm{AMOC}}}{h_{\mathrm{strat}}}} \right]. \end{aligned} \tag{10}$$

Thus, the volume transport of the AMOC depends on the same parameters and function as in (7) for the ACC, but the function involves the ratio $h_{\mathrm{AMOC}}/h_{\mathrm{strat}}$ rather than $h_{\mathrm{ACC}}/h_{\mathrm{strat}}$.

3.3. *Ratio of the ACC and AMOC volume transports*

Taking the ratio of the estimates of the magnitudes of the ACC and AMOC volume transports, (5) and (8), gives

$$\frac{T_{\mathrm{ACC}}}{T_{\mathrm{AMOC}}} = \frac{f_{\mathrm{AMOC}}}{|f_{\mathrm{ACC}}|} \frac{\left[1-\left(1+\frac{h_{\mathrm{ACC}}}{h_{\mathrm{strat}}}+\frac{h_{\mathrm{ACC}}^2}{2h_{\mathrm{strat}}^2}\right)e^{-\frac{h_{\mathrm{ACC}}}{h_{\mathrm{strat}}}}\right]}{\left[1-\left(1+\frac{h_{\mathrm{AMOC}}}{h_{\mathrm{strat}}}+\frac{h_{\mathrm{AMOC}}^2}{2h_{\mathrm{strat}}^2}\right)e^{-\frac{h_{\mathrm{AMOC}}}{h_{\mathrm{strat}}}}\right]}. \tag{11}$$

The Coriolis parameter is broadly similar within the ACC and at the southern tip of the Labrador Sea, given that we are neglecting variations in the former. Hence, the ratio of the volume transports of the ACC and AMOC is dominated by the second fraction involving just the ratios of the three depth scales, $h_{\mathrm{ACC}}/h_{\mathrm{strat}}$ and $h_{\mathrm{AMOC}}/h_{\mathrm{strat}}$. In the following section, we discuss the appropriate choices for each of these depths.

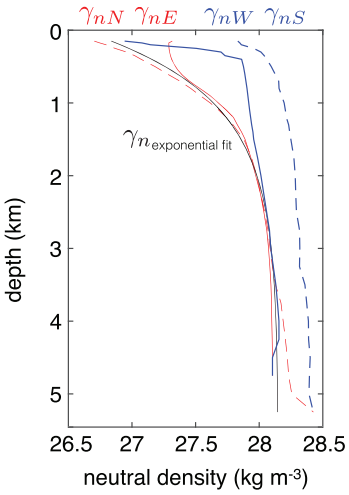

Fig. 6. Neutral density profiles along the sloping western (γ_{nW}) and eastern (γ_{nE}) boundaries at 50°N in the Atlantic (solid blue and red lines), along the sloping southern (γ_{nS}) and northern (γ_{nN}) boundaries at 18.5°E in the Southern Ocean (dashed blue and red lines), and the fitted exponential profile with $h_{\mathrm{strat}} = 0.9$ km (solid black line).

4. Selecting appropriate depth scales

4.1. *E-folding depth of the stratification, h_{strat}*

The prediction for the ratio of the ACC and AMOC volume transports (11) assumes a single value for the e-folding depth scale of the stratification, h_{strat}, along the eastern boundary of the Atlantic. To estimate this value, we fit an exponential profile in neutral density as in (3) to the WOCE climatological data of Gouretski and Koltermann (2004) at each location. The fit is achieved using a least squares regression. The upper 200 m of the water column is excluded from the fit in order to avoid the surface mixed layer. Across the majority of the ocean, an exponential profile is able to capture the majority of the observed vertical variation in density (not shown).

Figure 5 shows the e-folding depth (panel a), neutral density at the surface calculated using the fitted profile (panel b) and the asymptotic abyssal neutral density obtained by setting $z = -\infty$ (panel c). The reconstructed surface neutral density reveals the structure of the wind-driven gyres, as expected since no attempt is made to fit to the surface mixed layer where the neutral density profile is fundamentally at odds with an imposed exponential profile. Plotting the asymptotic abyssal neutral density is a useful consistency check on the approach since it should be near uniform, as indeed found in the Atlantic sector where our model is applied. The small increase in asymptotic abyssal neutral density across the Southern Ocean is likely associated with Antarctic Bottom Water formation.

Our best estimate of the e-folding depth in the Atlantic sector is $h_{\mathrm{strat}} = 0.9 \pm 0.2$ km. Significantly larger values are obtained within the Southern Ocean, consistent with the earlier findings of Kartsen and Marshall (2002), but these are not required by our thermal wind-based prediction for the ratio of the ACC and AMOC volume transports (11).

Figure 6 shows neutral density profiles along the sloping western and eastern boundaries at 50°N in the Atlantic and along the sloping southern and northern boundaries at 18.5°E in the Southern Ocean, the latter being chosen as the southern tip of the Atlantic's eastern boundary. Also plotted is the exponential fit to the stratification on the eastern boundary. The two climatological eastern boundary neutral density profiles (γ_{nN} and γ_{nE}) closely track both each other and the fitted exponential profile, except near the surface due to convection in the North Atlantic, and at depth in the Southern Ocean due to the gradient in bottom neutral density shown in Fig. 5c. This illustrates that our assumptions of (a) flat isopycnals along the eastern boundary of the Atlantic, and (b) an exponential dependence of density on depth, are reasonable.

The change in abyssal neutral density across the Southern Ocean means that neutral density at the southern boundary (γ_{nS}) is slightly greater in the observations than in our simple model, and not quite uniform with depth as we assume, but rather shows a modest decrease with height. Likewise, on the western boundary of the North Atlantic, the observed variation of neutral density with depth (γ_{nW}) is more complicated than the uniform value assumed in our simple model, as discussed in Section 3.2, but our imposed uniform value above the depth $z = -h_{\mathrm{AMOC}}$ is broadly consistent with the observed mean neutral density within this layer.

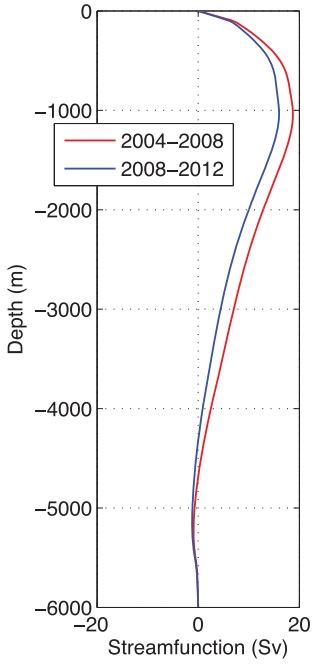

Fig. 7. AMOC streamfunction profiles (Sv) at 26.5N for the periods April 2004 to March 2008 and April 2008 to March 2012. Reproduced with permission from Smeed et al. (2014) under the Creative Commons Attribution 3.0 License.

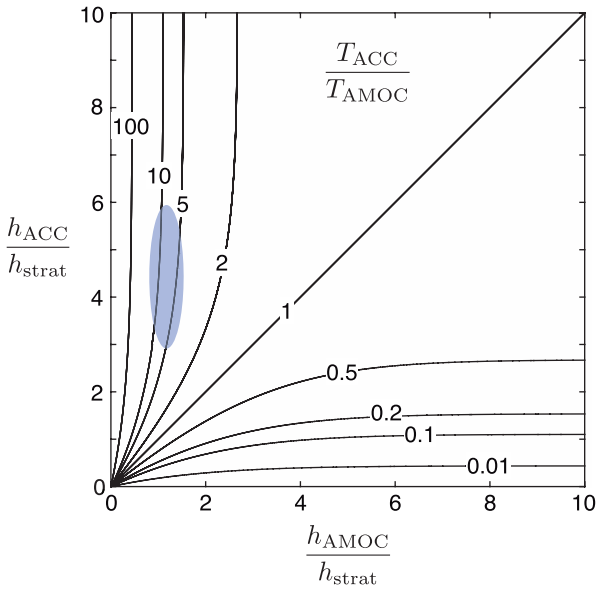

Fig. 8. Contours of $T_{\rm ACC}/T_{\rm AMOC}$ as a function of the two depth-scale ratios, $h_{\rm AMOC}/h_{\rm strat}$ and $h_{\rm ACC}/h_{\rm strat}$. The blue shading indicates the observation-based estimates of the depth-scale ratios, from which we infer $T_{\rm ACC}/T_{\rm AMOC} = 8 \pm 4$, consistent with the observed value of 8 ± 2.

4.2. *Depth of the ACC, $h_{\rm ACC}$*

There are several reasonable strategies for selecting the depth of the ACC, $h_{\rm ACC}$. One strategy might be to set $h_{\rm ACC}$ equal to the depth at which circumpolar flow is obstructed by bottom topography, which would be between 2 and 3 km. However, it is clear from climatological observations of active and passive tracers that there is circumpolar connectivity at greater depths (see Koltermann et al., 2011). As clear from all three hydrographic sections across the ACC in Fig. 2, the thermal wind extends down to around 4 km. Hence we set $h_{\rm ACC} = 4 \pm 1$ km.

4.3. *Depth of maximum overturning streamfunction, $h_{\rm AMOC}$*

The most reliable observations of the AMOC have been obtained at 26.5N under the RAPID-MOCHA programme. The vertical profile of the AMOC streamfunction as estimated by the RAPID-MOCHA array is reproduced in Fig. 7 from Smeed et al. (2014), averaged over two four year windows. Based on this data, our best estimate of the depth of maximum overturning streamfunction is $h_{\rm AMOC} = 1.1 \pm 0.2$ km, with the relatively large error bar chosen to reflect uncertainty arising from the application of data from 26.5N to the southern tip of the Labrador Sea.

5. Ratio of ACC and AMOC volume transports

The observed ratio of the ACC and AMOC volume transports, based on the values of Meredith et al. (2011) and Smeed et al. (2014) quoted in Section 1, is $(T_{\rm ACC}/T_{\rm AMOC})_{\rm observed} = 8 \pm 2$. This is now compared with our best estimate from the thermal wind-based relationship derived in Section 3.

In Fig. 8, we plot the variation of $T_{\rm ACC}/T_{\rm AMOC}$ with the two depth-scale ratios, $h_{\rm AMOC}/h_{\rm strat}$ and $h_{\rm ACC}/h_{\rm strat}$, as predicted by the thermal wind model (11). When these ratios are equal, as in the Gnanadesikan (1999) model, the ACC and AMOC volume transports are equal. More realistically, when $h_{\rm AMOC} \ll h_{\rm ACC}$, i.e. when the neutral density surfaces in the North Atlantic outcrop from shallower depths than those in the Southern Ocean, the ACC volume transport exceeds the AMOC volume transport.

From our best estimates of the three depth scales (Section 4), we have $h_{\rm ACC}/h_{\rm strat} = 4.4 \pm 1.5$ and $h_{\rm AMOC}/h_{\rm strat} = 1.22 \pm 0.35$. This region of parameter space is shaded in blue in Fig. 8. In this region, the variation of $T_{\rm ACC}/T_{\rm AMOC}$ is highly nonlinear: it is relatively insensitive to the maximum depth of the ACC, but highly sensitive to the ratio of the depth scales of the maximum AMOC streamfunction and stratification. From this figure, the best estimate of the ratio of the ACC and AMOC volume transports is in the range $T_{\rm ACC}/T_{\rm AMOC} = 8 \pm 4$. While the uncertainty is large, this value is consistent with the observed value of 8 ± 2.

On the other hand, the ratio of the ACC and AMOC volume transport calculated using the central estimates of $h_{\rm ACC}/h_{\rm strat}$

$= 4.4$ and $h_{\mathrm{AMOC}}/h_{\mathrm{strat}} = 1.2$ gives $T_{\mathrm{ACC}}/T_{\mathrm{AMOC}} = 6.6$, slightly smaller than the mean of the value quoted above, reflecting the nonlinearity in the relation between the volume transport ratio and $h_{\mathrm{AMOC}}/h_{\mathrm{strat}}$; this value is also smaller than that observed, but consistent within uncertainties. We note in passing that for parameter choices, $g = 9.8\,\mathrm{m^2\,s^{-1}}$, $(\Delta\gamma)_0 = 1.55\,\mathrm{kg\,m^{-3}}$, $\rho_0 = 1027\,\mathrm{kg\,m^{-3}}$ and $f_{\mathrm{AMOC}} = |f_{\mathrm{ACC}}| = 10^{-4}\,\mathrm{s^{-1}}$, equations (7) and (10) suggest $T_{\mathrm{AMOC}} = 16\,\mathrm{Sv}$ and $T_{\mathrm{ACC}} = 103\,\mathrm{Sv}$, the latter being slightly smaller than observed.

6. Concluding discussion

We have derived a simple relationship, based on thermal wind, for the relative magnitude of the volume transports of the AMOC and ACC. Required as inputs are just two non-dimensional parameters corresponding to the relative depths of the maximum AMOC streamfunction, the depth of the ACC and the e-folding depth of the Atlantic stratification. This thermal wind model succeeds in explaining why the mean ACC volume transport is roughly a factor eight times greater than the mean AMOC volume transport. Moreover, these three depth scales are easily diagnosed from model data and we suggest might be routinely diagnosed as metrics for ocean circulation model inter-comparison and validation.

It is particularly interesting that the ocean resides in a region of parameter space where the relative strength of the ACC and AMOC is insensitive to the ratio of the depth of the ACC and the e-folding depth, but acutely sensitive to the ratio of the depth of maximum AMOC streamfunction and the e-folding depth. This latter result suggests that subtle differences between the depth of maximum overturning and the e-folding depth of the stratification are particularly important. We note, for example, that the difference between these two depth scales cannot be resolved in layered models such as those developed by Radko and Kamenkovich (2011), Nikurashin and Vallis (2012), and Shakespeare and Hogg (2012).

The diagnostic relationship has many limitations. Firstly, while the stratification can be adequately modelled as exponential in the Atlantic sector to leading order, this is clearly an approximation. There is no fundamental fluid-dynamical constraint that requires the stratification to be exponential: see Vallis (2000) for examples of non-exponential stratification in the limit of low diapycnal diffusion; however, the exponential stratification does allow us to derive the simple relation for the relative strength of the ACC and AMOC in terms of the ratios of just three depth scales. Secondly, the depth of maximum overturning streamfunction in the North Atlantic is not a level of no motion at all longitudes, as assumed here. Thirdly, the Coriolis parameter varies across the ACC, although this introduces only a relatively small uncertainty of around 10% (Allison, 2009). And fourthly, the density is not uniform at the western boundary above the depth of maximum overturning streamfunction south of the Labrador Sea. Nevertheless, despite its simplicity, the model is able to explain the relative magnitudes of these two key ocean currents. We caution that the results in this manuscript apply only to the equilibrium ocean circulation, i.e. on millennial time scales (Allison et al., 2011; Jones et al., 2011; Samelson, 2011) and not to variability in the ACC and AMOC on centennial and shorter time scales.

A potential application of our results is to past climates. The continental geometry and depth of circumpolar connection are known to have varied (Barker and Thomas, 2004; Livermore et al., 2005), and this affects the volume transport of the ACC (e.g. Munday et al., 2015). It would be interesting to explore the variations of the ACC and AMOC volume transports in parallel across geological time in a series of numerical calculations with ocean circulation models.

Acknowledgements

The exponential fit to the WOCE climatology was performed using the ezyfit toolbox for Matlab developed by Frédéric Moisy to whom we are grateful. We also wish to thank three anonymous reviewers whose comments led to a much improved manuscript.

Disclosure statement

No potential conflict of interest was reported by the authors.

Funding

Partial financial support was provided by the UK Natural Environment Research Council [NE/K010948/1].

References

Allison, L. C. 2009. *Spin-Up and Adjustment of the Antarctic Circumpolar Current and Global Pycnocline*. PhD Thesis, University of Reading, 215 pp.

Allison, L. C., Johnson, H. L. and Marshall, D. P. 2011. Spin-up and adjustment of the Antarctic Circumpolar Current and global pycnocline. *J. Mar. Res.* **69**, 167–189.

Allison, L. C., Johnson, H. L., Marshall, D. P. and Munday, D. R. 2010. Where do winds drive the Antarctic Circumpolar Current? *Geophys. Res. Lett.* **37**, L12605. DOI: 10.1029/2010GL043355.

Barker, P. F. and Thomas, E. 2004. Origin, signature and palaeoclimatic influence of the Antarctic Circumpolar Current. *Earth Sci. Rev.* **66**, 143–162.

Cunningham, S. A., Kanzow, T., Rayner, D., Baringer, M. O., Johns, W. E. and co-authors. 2007. Temporal variability of the Atlantic meridional overturning circulation at 26.5^{circ}N. *Science* **317**, 935–938.

Gnanadesikan, A. 1999. A simple predictive model of the structure of the oceanic pycnocline. *Science* **283**, 2077–2081.

Gnanadesikan, A. and Hallberg, R. W. 2000. On the relationship of the circumpolar current to southern hemisphere winds in coarse-resolution ocean models. *J. Phys. Oceanogr.* **30**, 2013–2034.

Gouretski, V. V. and Koltermann, K. P. 2004. *WOCE global hydrographic climatology*. Vol. 35, Berichte des Bundesamtes fur Seeschifffahrt und Hydrographie, 52 pp.

Johns, W. E., Baringer, M. O., Beal, L. M., Cunningham, S. A., Kanzow, T. and co-authors. 2011. Continuous, array-based estimates of Atlantic ocean heat transport at 26.5°N. *J. Phys. Oceanogr.* **41**, 2429–2249.

Johnson, H. L., Marshall, D. P. and Sproson, D. A. J. 2007. Reconciling theories of a mechanically driven meridional overturning circulation with thermohaline forcing and multiple equilibria. *Clim. Dynam.* **29**, 821–836.

Jones, D. C., Ito, T. and Lovenduski, N. 2011. The transient response of the Southern Ocean pycnocline to changing atmospheric winds. *Geophys. Res. Lett.* **38**, L15604. DOI: 10.1029/2011GL048145.

Kartsen, R. H. and Marshall, J. 2002. Testing theories of the vertical stratification of the ACC against observations. *Dyn. Atmos. Oceans* **36**, 233–246.

Koltermann, K. P., Gouretski, V. V. and Jancke, K. 2011. Hydrographic Atlas of the World Ocean Circulation Experiment (WOCE). In: *Atlantic Ocean* (eds. M. Sparrow, P. Chapman and J. Gould) Vol. 3, Southampton, UK, International WOCE Project Office, ISBN 090417557X.

Livermore, R., Nankivell, A., Eagles, G. and Morris, P.. 2005. Paleogene opening of Drake Passage. *Earth Planet. Sci. Lett.* **236**, 459–470.

Lumpkin, R. and Speer, K. 2007. Global ocean meridional overturning. *J. Phys. Oceanogr.* **37**, 2550–2562.

Marshall, D. P. and Johnson, H. L. 2013. Propagation of meridional circulation anomalies along western and eastern boundaries. *J. Phys. Oceanogr.* **43**, 2699–2717

McCarthy, G. D., Smeed, D. A., Johns, W. E., Frajka-Williams, E., Moat, B. I. and co-authors. 2015. Measuring the Atlantic Meridional Overturning Circulation at 26°N. *Prog. Oceanogr.* **130**, 91–111.

Meredith, M. P., Woodworth, P. L., Chereskin, T. K., Marshall, D. P., Allison, L. C. and co-authors. 2011. Sustained monitoring of the Southern Ocean at Drake Passage: Past achievements and future priorities. *Rev. Geophys.* **49**, RG4005. DOI: 10.1029/2010RG000348.

Munday, D. R., Allison, L. C., Johnson, H. L. and Marshall, D. P. 2011. Remote forcing of the Antarctic Circumpolar Current by diapycnal mixing. *Geophys. Res. Lett.* **38**, L08609. DOI: 10.1029/2011GL046849.

Munday, D. R., Johnson, H. L. and Marshall, D. P. 2015. The role of ocean gateways in the dynamics and sensitivity to wind stress of the early Antarctic Circumpolar Current. *Paleoceanography* **30**, 284–302.

Nikurashin, M. and Vallis, G. 2012. A theory of the interhemispheric meridional overturning circulation and associated stratification. *J. Phys. Oceanogr.* **42**, 1652–1667.

Radko, T. and Kamenkovich, I. 2011. Semi-adiabatic model of the deep stratification and meridional overturning. *J. Phys. Oceanogr.* **41**, 757–780.

Samelson, R. M. 2011. Time-dependent adjustment in a simple model of the mid-depth meridional overturning cell. *J. Phys. Oceanogr.* **41**, 1009–1025.

Shakespeare, C. J. and Hogg, A. M. 2012. An analytical model of the response of the meridional overturning circulation to changes in wind and buoyancy forcing. *J. Phys. Oceanogr.* **42**, 1270–1287.

Sime, L. C., Stevens, D. P., Heywood, K. J. and Oliver, K. I. 2006. A decomposition of the Atlantic Meridional Overturning. *J. Phys. Oceanogr.* **36**, 2253–2270.

Smeed, D. A., McCarthy, G. D., Cunningham, S. A., Frajka-Williams, E., Rayner, D. and co-authors. 2014. Observed declined of the Atlantic Meridional Overturning Circulation 2004–2012. *Ocean Sci.* **10**, 29–38.

Trenberth, K. E. and Caron, J. M. 2001. Estimates of meridional atmosphere and ocean heat transports. *J. Climate* **14**, 3433–3443.

Vallis, G. K. 2000. Large-scale circulation and production of stratification: effects of wind, geometry and diffusion. *J. Phys. Oceanogr.* **30**, 933–954.